Original research article manuscript

(Published form available from: *Journal of The Mechanical Behavior of Biomedical Materials*, Pub Date : 2018-02-03, DOI: 10.1016/j.jmbbm.2018.01.025)

A novel fracture mechanics model explaining the axial penetration of bone-like porous, compressible solids by various orthopaedic implant tips

Sloan A. Kulper,[1] KY Sze,[2] Christian X. Fang,[1] Xiaodan Ren,[3] Margaret Guo,[4] Kerstin Schneider,[5] Frankie Leung,[1] William Lu,[1] Alfonso Ngan[2]

[1]Department of Orthopaedics & Traumatology, Li Ka Shing Faculty of Medicine, The University of Hong Kong, Hong Kong, China; [2]Department of Mechanical Engineering, Faculty of Engineering, The University of Hong Kong, Hong Kong, China; [3]School of Civil Engineering, Tongji University, Shanghai, China; [4]Stanford University School of Medicine, Stanford, USA; [5]Schulthess Clinic Zurich, Zurich, Switzerland. [6]Shenzhen Key Laboratory for Innovative Technology in Orthopaedic Trauma, The University of Hong Kong-Shenzhen Hospital, Shenzhen, China.

Corresponding Author:

Dr. Christian Fang, FRCS

Clinical Assistant Professor

Department of Orthopaedics and Traumatology, Queen Mary Hospital

The University of Hong Kong

Tel: +(852) 22554581 Fax: +(852) 28174392

E-mail address: cfang@hku.hk

Conflicts of Interest: Portions of the work presented here pertaining to elastomeric-tipped implants are patent-pending via The University of Hong Kong.

Running Title: Fracture mechanics of porous bone-like solids

Keywords: Fracture mechanics; trabecular bone; biomechanics; implant stability

Word Count: ~4,300 (Introduction/Body/References, excluding tables and figures)

Abstract

Many features of orthopaedic implants have been previously examined regarding their influence on migration in trabecular bone under axial loading, with screw thread design being one of the most prominent examples. There has been comparatively little investigation, however, of the influence that implant tip design has on migration under axial loads. We present a novel fracture mechanics model that explains how differences in tip design affect the force required for axial penetration of porous, compressible solids similar to trabecular bone. Three tip designs were considered based on typical 5 mm diameter orthopaedic locking screws: flat and conical tip designs, as well as a novel elastomeric tip.

Ten axial penetration trials were conducted for each tip design. In order to isolate the effect of tip design on axial migration from that of the threads, smooth steel rods were used. Tip designs were inserted into polyurethane foam commonly used to represent osteoporotic trabecular bone tissue (ASTM Type 10, 0.16 g/cc) to a depth of 10 mm at a rate of 2 mm/min, while force and position were recorded. At maximum depth, elastomeric tips were found to require the greatest force for axial migration (mean of 248.24 N, 95% Confidence Interval [CI]: 238.1–258.4 N), followed by conical tips (mean of 143.46 N, 95% CI: 142.1–144.9 N), and flat tips (mean of 113.88 N, 95% CI: 112.2–115.5 N). This experiment was repeated in cross-section while recording video of material compaction through a transparent window. Strain fields for each tip design were then generated from these videos using digital image correlation (DIC) software.

A novel fracture mechanics model, combining the Griffith with porous material compaction, was developed to explain the performance differences observed between the three tip designs. This model predicted that steady-state stress would be roughly the same (~4 MPa) across all designs, a finding consistent with the experimental results. The model also suggested that crack formation and friction are negligible mechanisms of energy absorption during axial penetration of porous compressible solids similar to trabecular bone. Material compaction appears to be the dominant mechanism of energy absorption, regardless of tip design. The cross-sectional area of the compacted material formed during migration of the implant tip during axial penetration was shown to be a strong determinant of the force required for migration to occur (Pearson Coefficient=0.902, $p<0.001$). As such, implant tips designed to maximize the cross-sectional area of compacted material – such as the elastomeric and conical tips in the present study – may be useful in reducing excessive implant migration under axial loads in trabecular bone.

1 Introduction

Rising rates of osteoporosis[1] place an increasing urgency on the development of fracture fixation implants that remain stable in bone of poor quality. Excessive implant migration following surgery remains a common post-surgical complication, including axial migration leading to cut-out.[2 3] Prior studies have examined many aspects of implant design related to migration within trabecular bone, such as damage to trabecular tissue during implantation surgery,[4] pull-out resistance of various thread designs,[5] stabilization using cement injection,[6] and the effect of bladed versus threaded implant designs on migration in osteoporotic tissue.[7] While the axial migration of complete implants has been examined in detail in numerous prior axial "push-out" studies,[8-11] the effect of implant tip design on axial migration has not been investigated. At present, surgeons and engineers lack concise explanations of why some implant tips penetrate bone more easily than others under axial loads.[12 13]

Fracture mechanics offers analytical tools that are relevant to implant stability. Following Griffith's 1921 publication[14] of a model predicting the crack depth needed to spontaneously shatter a material, subsequent researchers added theories for plasticity,[15] toughness,[16] and complex geometries.[17] In orthopaedics, fracture mechanics has been used to study topics such as microstructural damage[18] and energy at the implant-cement interface.[19] Additionally, models of bone strength[20 21] have been developed by combining simplified structures, pioneered by Gibson,[22] with detailed material data from cadaveric bone.[23] To the authors' knowledge, however, no analytical model presently exists to concisely explain why some tip designs require more force to penetrate trabecular bone than others. This may be due in part to the status of porous, compressible solids as a poorly understood class of materials in solid mechanics.[24] Prior osteopenetration and indentation studies[25 26] have focused on understanding bone as a material, rather than investigating implant tip performance. The hypothesis of the present study, therefore, is that development of an analytical model that

explains implant tip performance in trabecular bone may yield insights useful in clinical practice and implant design, particularly for patients with osteoporosis.

2 Materials and methods

2.1 Uniaxial Compression Experiment

To test the compressive behaviors of the substrate, four cubes measuring 19×19×19 mm were sawn from a 130×180×40 mm blocks of ASTM grade 10 (0.16 g/cc) polyurethane foam (Sawbones Europe AB, Malmö, Sweden). O'Neill et al.[11] showed that surrogate bone consisting of medium-density polyurethane foam (ASTM Type 10, 0.16 g/cc) provides useful results consistent with the performance of osteoporotic trabecular bone of the proximal femur when performing biomechanical testing of axial migration of hip implants, consistent with the results of prior studies into the mechanical properties of such materials.[27-30] Specimens were compressed to 50% height at a rate of 2 mm/min while recording force-displacement data using a mechanical testing machine (MTS 858 Mini Bionix with 1 kN loadcell, MTS, Inc., Minnesota, USA).

2.2 Axial Implant Tip Penetration and Visualization Experiments

Indenters were fabricated from 5 mm diameter 316L steel rods cut into 40 mm-long segments (Figure 1). They were then machined to add either a flat or a 55º conical (sharp) tip, similar in design to typical blunt or self-tapping cancellous screws, respectively. Twelve polymer tips were cut with a cannulated drill from a 5 mm thick 70A hardness PDMS sheet (McMaster-Carr, Chicago, USA). Foam blocks were marked with a 12.5×12.5 mm grid and 5.1 mm diameter holes were drilled at the center of each cell to 7 mm depth, into which indenters were placed. Specimens were then placed on the load cell platform, and indenters were displaced at 2 mm/min (consistent prior axial migration "push-out" studies)[11] to a depth

of 10 mm while recording force at 0.5 Hz, Ten trials were completed for each tip design, with polymer tips used only once.

Indenters and remaining polymer tips were then sawn in half longitudinally (Figure 2). New foam blocks were sawn into 25×25×40 mm specimens, and 5.1 mm diameter holes were drilled at the center of each 25×25 mm face to a depth of 7 mm. Each specimen was then cut in half, producing twelve total specimens measuring 12.5×25×40 mm, and newly exposed faces were airbrushed with black pigment for visual contrast. Each specimen was clamped with minimal force between transparent PMMA slides. Indenters were placed in each bisected hole, and then inserted into the foam substrate at 2 mm/min to 10 mm depth while video of the exposed face was recorded (Elphel NC353L, Elphel Inc, Utah, USA) at 2592x1936 resolution and 10 fps for compaction zone measurements, based on methods described for similar to those described by Kelly et al.[31] Four trials were completed for each tip design, with polymer tips used only once.

SPSS v24.0 (IBM, Armonk, NY, USA) was used to compare mean force-displacement values with 95% confidence intervals via Student's *t*-distribution. Force-displacement and compaction zone areas were compared between the three indenter tip designs using one-way ANOVA. A type one error rate of $p<0.05$ was taken as statistically significant.

2.3 Digital Image Correlation (DIC) Analysis and Analytical Modelling

To generate tip penetration strain fields, videos of the longitudinally-sawn indenter experiments were imported to an open-source DIC platform, NCorr v1.2.1 running in Matlab R2015b (The MathWorks, Inc., Massachusetts, USA). Images were cropped to a 17.5×17.5 mm region of interest (ROI) at half resolution (968×968) to reduce computational load.

Eulerian-Almansi YY and XY strain field were generated using standard settings (30 pixel ROI subsets with 5 pixel spacing).[32]

2.4 Fracture mechanics theory with novel model of porous material compaction

An analytical model of the experiment was developed to explain the mechanics of tip penetration. Total force applied by the indenter may be separated into force applied by either the side F_{side} or the tip F_{tip} , giving us:

$$\Sigma F = F_{side} + F_{tip} = \tau A_L + \sigma_c A_{tip} \qquad \text{(Eqn. 1)}$$

where τ is the shear stress, A_L is the area of the side of the indenter across the shear plane, σ_c is the compressive stress, and A_{tip} the tip area. Since in the experiment, side features such as screw threads were removed, we may assume that side forces (e.g. friction) are negligible (confirmed using strain field values in Eqn. 6 below).

For a bone-like substrate with thickness h and applied stress σ (Figure 3), the length of a tube-shaped crack c extending from the top surface of the specimen is equal to the sum of the penetration depth of the indenter and the height of the compacted zone of material c_c. Applying the concept of hardening by densification, the compacted zone is assumed to act like a rigid, fully-dense extension of the indenter.[33-35] We may therefore link the value of a to the growing radius of the compacted zone. Furthremote, assume that all material in this zone has been compressed to a constant compaction ratio ε_c:

$$\varepsilon_c = \frac{c - c_c}{c} \qquad \text{(Eqn. 2)}$$

For a small increase dc in crack length c, there are two potential mechanisms of energy absorption: crack surface formation energy U_{crack} and material compaction energy $U_{compact}$. The incremental energy absorbed by crack formation will be $4\pi a\gamma\, dc$, where γ is the material free surface energy with units of J/m^2. Assume that compaction occurs at a constant

material stress σ_0. For a layer of material with height dc, the energy absorbed by compaction is $\sigma_0 \pi a^2 \times (\varepsilon_c \, dc)$, where $\sigma_0 \pi a^2$ is the applied force and $\varepsilon_c \, dc$ is the displacement, equal to the distance of compaction for a layer with height dc. The total energy absorbed is therefore:

$$\Sigma U = U_{crack} + U_{compact} = 4\pi a\gamma \, dc + \sigma_0 \pi a^2 \varepsilon_c \, dc \qquad \text{(Eqn. 3)}$$

According to Griffith,[14] as the crack grows longer the total potential energy (strain energy) of the specimen decreases. When the depth of the crack c approaches the total specimen thickness h, piling theory predicts that elastic strain will occur within a nearly cylindrical volume of material of radius a and height $h - c$.[36 37] As an approximation, assume in this case that the stress applied to this zone equals the entire applied stress σ. Therefore, if elastic energy U_e is equal to the product of the elastic energy density f_e and the volume of the elastically strained region V_e:

$$U_e = f_e \times V_e = \left(\frac{\sigma^2}{2E}\right) \times [\pi a^2 (h - c)] \qquad \text{(Eqn. 4)}$$

where E is the Young's modulus of the material. If the crack length increases by an increment dc, the change in elastic energy will be:

$$\frac{dU_e}{dc} = \left(\frac{\sigma^2}{2E}\right) \times \pi a^2 dc \qquad \text{(Eqn. 5)}$$

A crack may grow without additional energy input once it surpasses a depth determined by the Griffith Criterion.[14] If we assume that these conditions are met in the experiment (confirmed by the asymptotic region of region of stress below), then the total energy absorption (Eqn. 3) must be equal to the amount of elastic energy released (Eqn. 5), or:

$$U_{crack} + U_{compact} = \frac{dU_e}{dc}$$

$$4\pi a\gamma \, dc + \sigma_0 \pi a^2 \varepsilon_c \, dc = \left(\frac{\sigma^2}{2E}\right) \times \pi a^2 dc \qquad \text{(Eqn. 6)}$$

Solving for the total stress σ, we have:

$$\sigma = \sqrt{2E\left(\frac{4\gamma}{a} + \sigma_0 \varepsilon_c\right)} \qquad \text{(Eqn. 6)}$$

3 Results

3.1 Results of Uniaxial Compression Experiment

Measurement of the linear region mean stress-displacement curve (Figure 4) showed a value of 2.2 MPa/mm, allowing us to calculate the Young's modulus as $2.2\,\frac{\text{MPa}}{\text{mm}} \times 19\text{mm} = 42\text{MPa}$, similar to the manufacturer-supplied value of 58 MPa. Steady-state stress (σ_0 in the model below) had a value of 2.2 MPa. (DiB article,[38] datasets 1.1.1 and 1.1.2)

3.2 Results of Implant Tip Penetration and Visualization Experiments

Mean forces required for penetration by full-diameter indenters (Figure 5) differed significantly between tip designs (one-way ANOVA, $p < 0.001$) (Table 1 and DiB article,[38] dataset 1.2.1), as did mean compaction zone areas (Figure 6) measured from video frames at 1mm depth increments ($p<0.001$, One-way ANOVA for each depth from 1 to 10 mm) (Table 2 and DiB article,[38] dataset 1.2.1). Flat-tipped indenters produced long, thin compaction zones of widths up to 135% tip diameter. Sharp-tipped indenters produced conical compaction zones with boundaries 1-1.5 mm offset from the tip of widths up to 160% tip diameter. Polymer-tipped indenters produced broad, semi-elliptical compaction zones with widths up to 185% tip diameter. Mean force was divided by compaction zone area to generated estimated stress-displacement curves with asymptotically convergent values ~4 MPa for all tip designs (Figure 7). Strong correlation (Pearson correlation coefficient = 0.902, $R^2=0.814$, $p<0.001$) was found between force and compaction zone area (Figure 8).

Table 1. Force-displacement values from implant tip penetration experiment (see DiB article,[38] dataset 1.2.1).

Force-Displacement Data							
	Flat tip force (N)		Sharp tip force (N)		Polymer tip force (N)		*p*-value
Depth (mm)	Mean (n=10)	95% CI	Mean (n=10)	95% CI	Mean (n=10)	95% CI	(one-way ANOVA)
1	62.42	59.2 - 65.7	28.59	26.6 - 30.6	18.77	12.8 - 24.8	<0.001
2	76.14	74.7 - 77.6	42.28	39.6 - 45	69.29	58 - 80.6	<0.001
3	82.18	80.8 - 83.6	62.33	58.8 - 65.9	120.92	115.6 - 126.2	<0.001
4	88.40	87.3 - 89.5	91.66	88 - 95.4	158.62	154.7 - 162.6	<0.001
5	92.31	91.2 - 93.4	106.99	105.1 - 108.9	189.25	185.3 - 193.2	<0.001
6	97.32	95.8 - 98.8	113.43	111.2 - 115.7	212.52	209.4 - 215.6	<0.001
7	102.06	99.3 - 104.8	121.46	119.7 - 123.2	228.78	222.3 - 235.2	<0.001
8	105.93	103 - 108.8	128.88	126.9 - 130.8	238.67	230 - 247.3	<0.001
9	110.57	107.9 - 113.2	135.59	134.3 - 136.8	242.77	234.2 - 251.4	<0.001
10	113.88	112.2 - 115.5	143.46	142.1 - 144.9	248.24	238.1 - 258.4	<0.001

Table 2. Compaction zone diameter values from implant tip penetration-visualization experiment (see DiB article,[38] dataset 1.2.1).

Compaction Zone Diameter-Displacement Data										
	Flat tip compaction zone diameter (mm)			Sharp tip compaction zone diameter (mm)			Polymer tip compaction zone diameter (mm)			*p*-value
Depth (mm)	Mean (n=4)	Min	Max	Mean (n=4)	Min	Max	Mean (n=4)	Min	Max	(one-way ANOVA)
1	5.08	5.00	5.15	1.54	1.50	1.65	5.13	5.10	5.15	<0.001
2	5.54	5.50	5.65	2.34	2.10	2.50	6.28	5.40	6.70	<0.001
3	5.94	5.85	6.00	3.90	3.70	4.15	6.88	5.75	7.50	<0.001
4	6.21	6.10	6.50	4.81	4.25	5.35	7.33	6.25	7.80	<0.001
5	6.34	6.20	6.65	5.24	4.95	5.75	7.94	7.00	8.25	<0.001
6	6.55	6.35	6.75	5.88	5.50	6.00	8.16	7.50	8.45	<0.001
7	6.65	6.45	6.75	6.18	6.00	6.40	8.35	8.00	8.50	<0.001
8	6.70	6.50	6.85	6.48	6.15	7.00	8.53	8.45	8.60	<0.001
9	6.75	6.60	6.95	6.86	6.15	8.00	8.74	8.50	9.00	<0.001
10	6.80	6.65	7.00	7.00	6.50	8.00	8.84	8.50	9.25	<0.001

3.3 Results of Digital Image Correlation Analysis and Analytical Modelling

Vertical (YY) strain fields (Figure 9 and DiB article,[38] dataset 1.3.1) revealed a maximum strain of approximately -5.0% at the indenter-compaction zone interface for all tip designs (the compaction ratio ε_c, mentioned in the model below) . This high strain region was concentrated along a band near the edge of flat-tipped indenters. Polymer-tipped indenters produced similar, though wider, high strain regions. Sharp-tipped indenters produced semi-circular bands of high strain surrounding the tip point. Shear (XY) strain fields (Figure 10 and DiB article,[38] dataset 1.3.1) revealed large regions of low-intensity ($\pm 0.5\%$) shear strain radiating away from the distal edge of the compaction zones of all tip designs. Shear strain values along the sides of the indenter were very low ($\pm 0.1\%$), indicating little to no side friction.

The analytical model predicts that while stress is independent of both depth c and thickness h (Eqn. 7), it is inversely related to the compaction zone radius a. Experimentally, we observed that while the compaction zone grew along with force (Figure 8 and DiB article,[38] dataset 1.2.1), total stress approached a constant value (Figure 7). This suggests that the crack formation term ($\frac{4\gamma}{a}$) has a negligible effect on stress and may be eliminated. If we then substitute in the experimentally-determined values for Young's Modulus E, material stress σ_0, and compaction ratio ε_c, we have:

$$\sigma \approx \sqrt{2E\sigma_0\varepsilon_c} \approx \sqrt{2 \times 42\ \text{MPa} \times 2.2\ \text{MPa} \times 0.05} = 3.09\ \text{MPa}$$

Using the manufacturer-supplied Young's Modulus of 58 MPa to define an upper bound for our prediction, we have $\sigma = 3.57$ MPa. Elimination of the crack formation term appears justified when we retain $\frac{\gamma}{a}$ in Eqn. 3 and use the mean Young's Modulus of 50 MPa:

$$\sigma = \sqrt{2E\left(\frac{4\gamma}{a} + \sigma_0\varepsilon_c\right)} = 3.32\ \text{MPa} = \sqrt{2\ \times\ 50\ \text{MPa}\ \times\left(\frac{4\gamma}{a} + 2.2\ \text{MPa}\ \times\ 0.05\right)}$$

Crack formation therefore had a very small effect ($\frac{\gamma}{a} =$ 0.60 kPa) on the total stress compared to material compaction ($\sigma_0\varepsilon_c \approx 110$ kPa).

In summary, the predicted value range ($3.09 - 3.57$ MPa) nearly matched the experimental value for all three indenter tip designs (Figure 7 and DiB article,[38] dataset 1.2.1), suggesting that the model is valid.

4 Discussion

The objective of this study was to develop a novel fracture mechanics model capable of explaining how differences in tip design affect the force required for axial penetration of porous, compressible solids similar to trabecular bone. The results suggest that this model accurately represents the fracture and compaction behavior observed during the empirical phase of the present study; predicted stress ($3.09 - 3.57$ MPa) nearly matched the experimental value for all three indenter tip designs (Figure 7 and DiB article,[38] dataset 1.2.1), despite significant variations between these designs in terms of tip geometry, material properties, and resulting migration force. The model also ranked the relative importance of various energy absorption mechanisms during axial penetration, suggesting that crack formation and friction are negligible energy absorption mechanisms (<0.5% of the total) compared to material compaction, regardless of tip design. This insight may useful to biomedical engineers when designing implants to resist migration under axial loads, as attention may be focused on developing tip designs that maximize material compaction rather than other energy absorption mechanisms.

Three tip designs were considered based on typical 5 mm diameter orthopaedic locking screws: flat and conical tip designs, as well as a novel elastomeric tip. Flat and sharp tips

were designed to approximate standard blunt and self-tapping orthopaedic screws[39] with abstract cylindrical and conical forms, facilitating the use of concepts from piling theory.[36] Polymer tips were deemed appropriate for inclusion based on pilot study results suggesting excellent resistance to axial penetration. The inclusion of elastically-deformable tips also tested the model's ability to explain the performance of a wider range of potential tip designs.

In the interest of reproducibility, standard orthopaedic-grade[40] ASTM Type 10 0.16 g/cc polyurethane foam was chosen as a surrogate for osteoporotic trabecular bone of the proximal femur based on prior validation. [11] While the use of a bone surrogate may be seen as a limitation of the present study, the work of O'Neill et al.[11] provides strong justification establishing its validity as a predictor of osteoporotic trabecular bone behavior in similar "push in" experiments.[8-10] O'Neill found 0.16 g/cc polyurethane foam provided excellent predictions of the axial penetration of osteoporotic trabecular bone from the human proximal femur,[11] under loading conditions very similar to the present study. In the present study, specimen size and grid spacing was in excess of the twice-diameter spacing used by Hvid et al.[41 42] to eliminate the risk of significant interactions between adjacent axial penetration trials.

In order to isolate the effect of tip design on axial migration from that of the threads, smooth steel rods were used. While useful to simplify analysis for the purpose of constructing the fracture mechanics model, this represents a potential limitation of the study. Further research is required to examine how the material fracture and compaction behavior of the tip is affected by the presence of threads and other implant features. Likewise, higher-than-predicted values of stress for sharp and polymer-tipped indenters (10 and 25%, respectively) may be the result of a failure to account for energy absorption occurring outside the compaction zone. Simulation may be a useful supplement to algebraic modelling in further study due to the geometric complexity of these problems.

The cross-sectional area of the compacted material formed during migration of the implant tip during axial penetration was found to be a strong determinant of the force required for migration to occur (Pearson Coefficient=0.902, $p<0.001$). As such, implant tips designed to maximize the cross-sectional area of compacted material – such as the elastomeric and conical tips in the present study – may be useful in reducing excessive implant migration under axial loads in trabecular bone.

In clinical practice, it is preferable to minimize post-surgical implant migration. The results of the present study suggest that bone compaction near the implant tip improves stability under axial loading conditions. All tip designs in this study required at least several millimeters of sacrificial material to develop compaction zones wide enough to substantially increase resistance to axial loading. Clinically, this may be achieved by drilling a shallow pilot hole, and then compacting excess material as the implant is inserted to the depth required for reduction. Flat tip compaction zones grew most quickly, but had low upper-bounds for cross sectional area. They also extended far from the end of the tip, potentially posing a risk of causing cut-out in advance of the implant itself. Flat-tipped implants may therefore be useful in cases where bone is too strong to develop a large compaction zone during insertion, or when pilot holes must be drilled deeply, close to the cortex. Conversely, allowing a flat-tipped implant to compact more than a few millimeters of material may increase the risk of cut-out. Sharp tip compaction zones showed slow initial growth, but reached a relatively high maximum cross-sectional area after 4-5 mm of penetration. Sharp-tipped implants may be useful in improving axial stability in cases where pilot holes may be drilled initially shallow, and bone is of sufficiently poor quality that the excess trabecular tissue can be readily crushed by the tip during insertion. Polymer tips produced little material damage initially, as energy was absorbed into elastic compression, and lateral expansion, of the polymer itself. Compaction zones grew quickly beyond 2 mm depth, leading this design

to achieve the greatest axial stability in the study. Polymer-tipped indenters may be useful, therefore, in two scenarios: (1) when there is insufficient trabecular tissue to develop a stabilizing compaction zone, such as when implants are placed deeply (near the relatively dense subchondral/cortical layers), or (2) when implants are inserted into bone of poor quality, such as osteoporotic bone.

5 Acknowledgements

We would like to thank Prof. Mingxin Huang, Mr. Zhichao Luo, Mr. Stephen Chan, and Ms. Jessica Kabigting of the University of Hong Kong, as well as Ms. Minsoo Khang of the Massachusetts Institute of Technology, for their assistance related to instrumentation and data collection for this paper. This work was funded in part by the Hong Kong Innovation and Technology Fund [grant number ITS/171/15FP], and the Hong Kong PhD Fellowship [award number PF12-16873]. Portions of the work presented here pertaining to polymer-tipped implants are patent-pending via The University of Hong Kong.

6 References

1. Johnell O, Kanis JA. An estimate of the worldwide prevalence and disability associated with osteoporotic fractures. *Osteoporos Int* 2006;17(12):1726-33.

2. Kanis JA, Oden A, McCloskey EV, et al. A systematic review of hip fracture incidence and probability of fracture worldwide. *Osteoporos Int* 2012;23(9):2239-56.

3. Baumgaertner MR, Curtin SL, Lindskog DM, et al. The value of the tip-apex distance in predicting failure of fixation of peritrochanteric fractures of the hip. *JBJS* 1995;77(7):1058-64.

4. Ryan MK, Mohtar AA, Cleek TM, et al. Time-elapsed screw insertion with microct imaging. *J Biomech* 2016;49(2):295-301.

5. Damm NB, Morlock MM, Bishop NE. Influence of trabecular bone quality and implantation direction on press-fit mechanics. *J Orthop Res* 2017;35(2):224-33.

6. Leichtle CI, Lorenz A, Rothstock S, et al. Pull-out strength of cemented solid versus fenestrated pedicle screws in osteoporotic vertebrae. *Bone Joint Res* 2016;5(9):419-26.

7. Sommers MB, Roth C, Hall H, et al. A laboratory model to evaluate cutout resistance of implants for pertrochanteric fracture fixation. *J Orthop Trauma* 2004;18(6):361-8.

8. Aminian A, Gao F, Fedoriw WW, et al. Vertically oriented femoral neck fractures: Mechanical analysis of four fixation techniques. *J Orthop Trauma* 2007;21(8):544-8.

9. Richards R, Evans G, Egan J. The ao dynamic hip screw and the pugh sliding nail in femoral head fixation. *Bone & Joint Journal* 1990;72(5):794-96.

10. Rosenblum SF, Zuckerman JD, Kummer F, et al. A biomechanical evaluation of the gamma nail. *Bone & Joint Journal* 1992;74(3):352-57.

11. O'Neill F, Condon F, McGloughlin T, et al. Validity of synthetic bone as a substitute for osteoporotic cadaveric femoral heads in mechanical testing a biomechanical study. *Bone & Joint Research* 2012;1(4):50-55.

12. Li B, Aspden RM. Composition and mechanical properties of cancellous bone from the femoral head of patients with osteoporosis or osteoarthritis. *J Bone Miner Res* 1997;12(4):641-51.

13. Gefen A. Optimizing the biomechanical compatibility of orthopedic screws for bone fracture fixation. *Med Eng Phys* 2002;24(5):337-47.

14. Griffith AA. The phenomena of rupture and flow in solids. *Philosophical transactions of the royal society of london Series A, containing papers of a mathematical or physical character* 1921;221:163-98.

15. Irwin GR. Analysis of stresses and strains near the end of a crack traversing a plate. *Journal of applied mechanics* 1957;24(3):361-64.

16. A path independent integral and the approximate analysis of strain concentration by notches and cracks; 1968. ASME.

17. Xu X-P, Needleman A. Numerical simulations of fast crack growth in brittle solids. *Journal of the Mechanics and Physics of Solids* 1994;42(9):1397-434.

18. Guo X-DE, McMahon TA, Keaveny TM, et al. Finite element modeling of damage accumulation in trabecular bone under cyclic loading. *Journal of Biomechanics* 1994;27(2):145-55.

19. Thompson JI, Gregson PJ, Revell PA. Analysis of push-out test data based on interfacial fracture energy. *J Mater Sci Mater Med* 1999;10(12):863-8.

20. Keaveny TM, Hayes WC. A 20-year perspective on the mechanical properties of trabecular bone. *J Biomech Eng* 1993;115(4B):534-42.

21. Wang J, Zhou B, Liu XS, et al. Trabecular plates and rods determine elastic modulus and yield strength of human trabecular bone. *Bone* 2015;72:71-80.

22. Gibson LJ. The mechanical-behavior of cancellous bone. *Journal of Biomechanics* 1985;18(5):317-&.

23. Lotz JC, Gerhart TN, Hayes WC. Mechanical properties of trabecular bone from the proximal femur: A quantitative ct study. *Journal of computer assisted tomography* 1990;14(1):107-14.

24. Ngan AHW. On the distribution of elastic forces in disordered structures and materials. I. Computer simulation. *Proceedings of the Royal Society A: Mathematical, Physical and Engineering Sciences* 2005;461(2054):433-58.

25. Frich LH, Jensen NC. Bone properties of the humeral head and resistance to screw cutout. *Int J Shoulder Surg* 2014;8(1):21-6.

26. Kelly N, Cawley DT, Shannon FJ, et al. An investigation of the inelastic behaviour of trabecular bone during the press-fit implantation of a tibial component in total knee arthroplasty. *Med Eng Phys* 2013;35(11):1599-606.

27. Cristofolini L, Viceconti M, Cappello A, et al. Mechanical validation of whole bone composite femur models. *Journal of biomechanics* 1996;29(4):525-35.

28. Heiner AD, Brown TD. Structural properties of a new design of composite replicate femurs and tibias. *J Biomech* 2001;34(6):773-81.

29. Agneskirchner J, Freiling D, Hurschler C, et al. Primary stability of four different implants for opening wedge high tibial osteotomy. *Knee surgery, sports traumatology, arthroscopy* 2006;14(3):291-300.

30. Peindl RD, Zura RD, Vincent A, et al. Unstable proximal extraarticular tibia fractures: A biomechanical evaluation of four methods of fixation. *Journal of orthopaedic trauma* 2004;18(8):540-45.

31. Kelly N, McGarry JP. Experimental and numerical characterisation of the elasto-plastic properties of bovine trabecular bone and a trabecular bone analogue. *J Mech Behav Biomed Mater* 2012;9:184-97.

32. Blaber J, Adair B, Antoniou A. Ncorr: Open-source 2d digital image correlation matlab software. *Experimental Mechanics* 2015;55(6):1105-22.

33. Szivek JA, Thomas M, Benjamin JB. Characterization of a synthetic foam as a model for human cancellous bone. *Journal of Applied Biomaterials* 1993;4(3):269-72.

34. Goldstein SA. The mechanical properties of trabecular bone: Dependence on anatomic location and function. *J Biomech* 1987;20(11-12):1055-61.

35. Gibson LJ. Biomechanics of cellular solids. *J Biomech* 2005;38(3):377-99.

36. Yu H, Mitchell J. Analysis of cone resistance: Review of methods. *Journal of Geotechnical and Geoenvironmental Engineering* 1998;124(2):140-49.

37. Salgado R, Mitchell JK, Jamiolkowski M. Cavity expansion and penetration resistance in sand. *Journal of Geotechnical and Geoenvironmental Engineering* 1997;123(4):344-54.

38. Kulper S, Sze K, Fang C, et al. Axial penetration of porous bone-like substrate with sharp/conical, flat, and polymer-tipped implant-like indenters. *Data in Brief* 2017;(under review)

39. Perren SM. Evolution of the internal fixation of long bone fractures - the scientific basis of biological internal fixation: Choosing a new balance between stability and biology. *Journal of Bone and Joint Surgery-British Volume* 2002;84b(8):1093-110.

40. ASTM Standard F1839-08, 2008, Standard specification for rigid polyurethane foam for use as a standard material for testing orthopaedic devices and instruments, ASTM International, West Conshohocken, PA, 2008, 10.1520/f1839-08r12, www.astm.org

41. Hvid I, Andersen K, Olesen S. Cancellous bone strength measurements with the osteopenetrometer. *Engineering in medicine* 1984;13(2):73-78.

42. Hvid I, Hansen SL. Trabecular bone strength patterns at the proximal tibial epiphysis. *Journal of orthopaedic research* 1985;3(4):464-72.

7 Figures

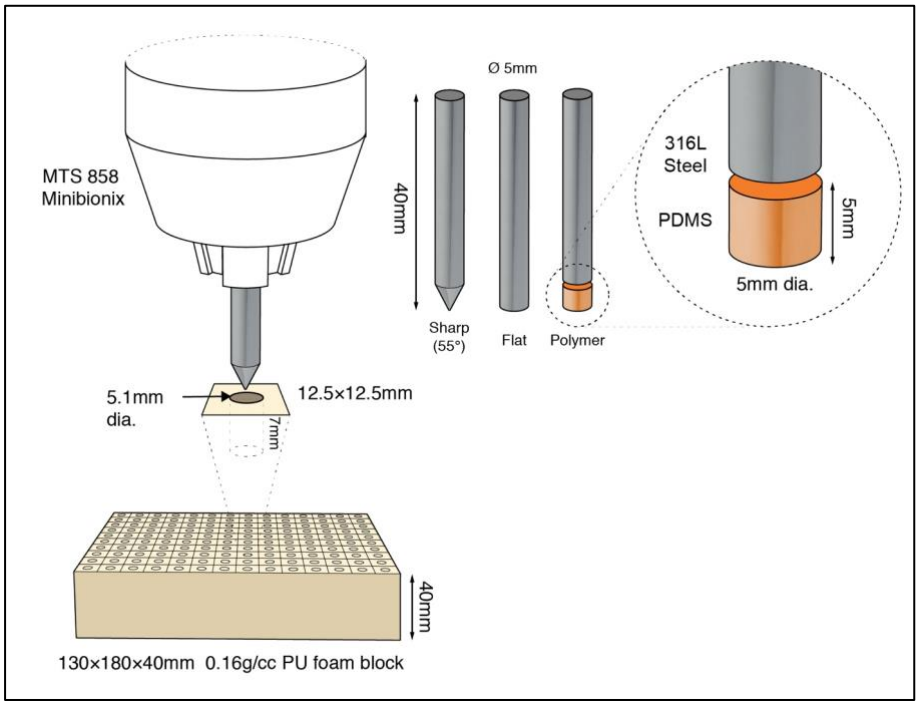

Figure 1. Illustration of axial implant tip penetration experiment. Force-displacement data was collected during penetration of polyurethane foam by flat, sharp, and polymer tip designs to a depth of 10 mm.

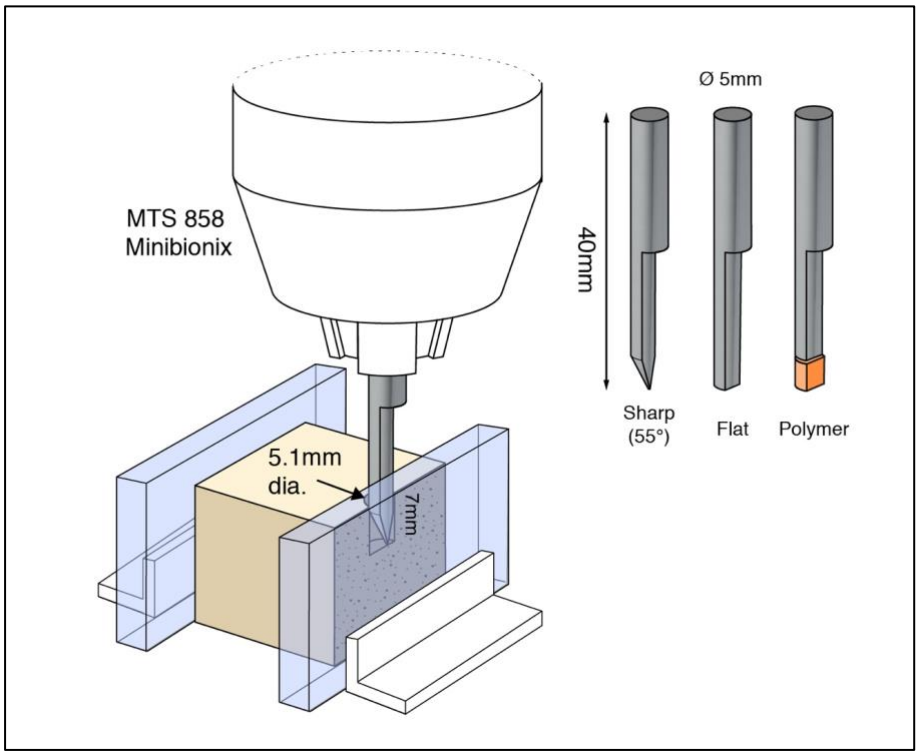

Figure 2. Illustration of axial implant tip penetration visualization experiment. Tip designs were sawn in half along their lengths in order to permit video recording for generation of strain fields using digital image correlation.

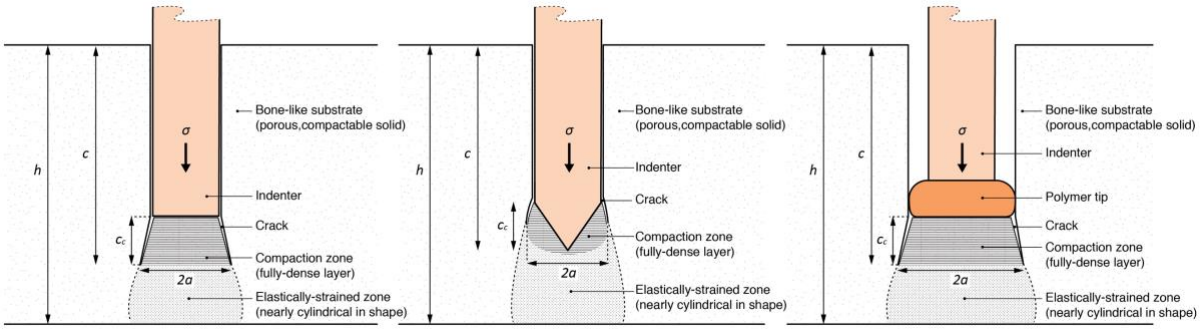

Figure 3. Diagram of analytical model used to explain differences in penetration performance between flat (left), sharp (middle), and polymer (right) tip designs.

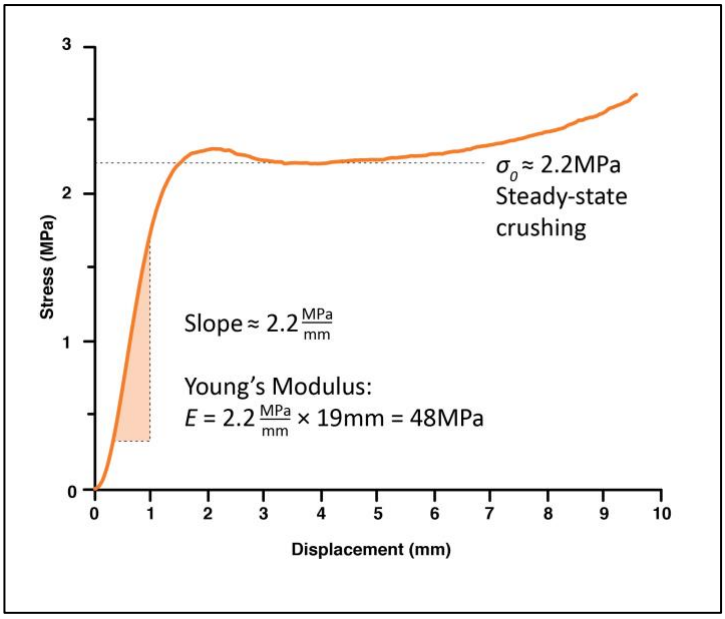

Figure 4. Stress-displacement curve from uniaxial compression experiment, showing estimates of Young's modulus and σ_0.

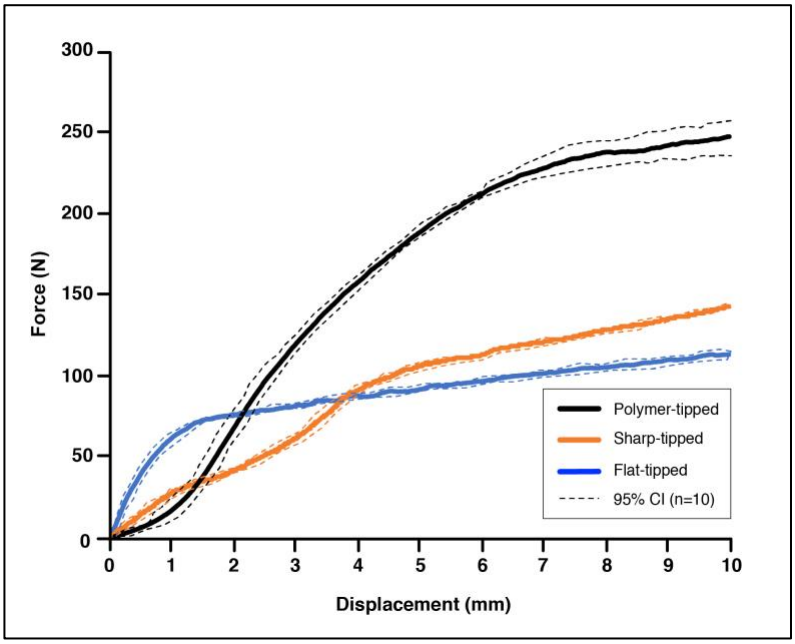

Figure 5. Force-displacement curves from implant penetration experiment (full-diameter), showing 95% confidence intervals for ten trials of each tip design.

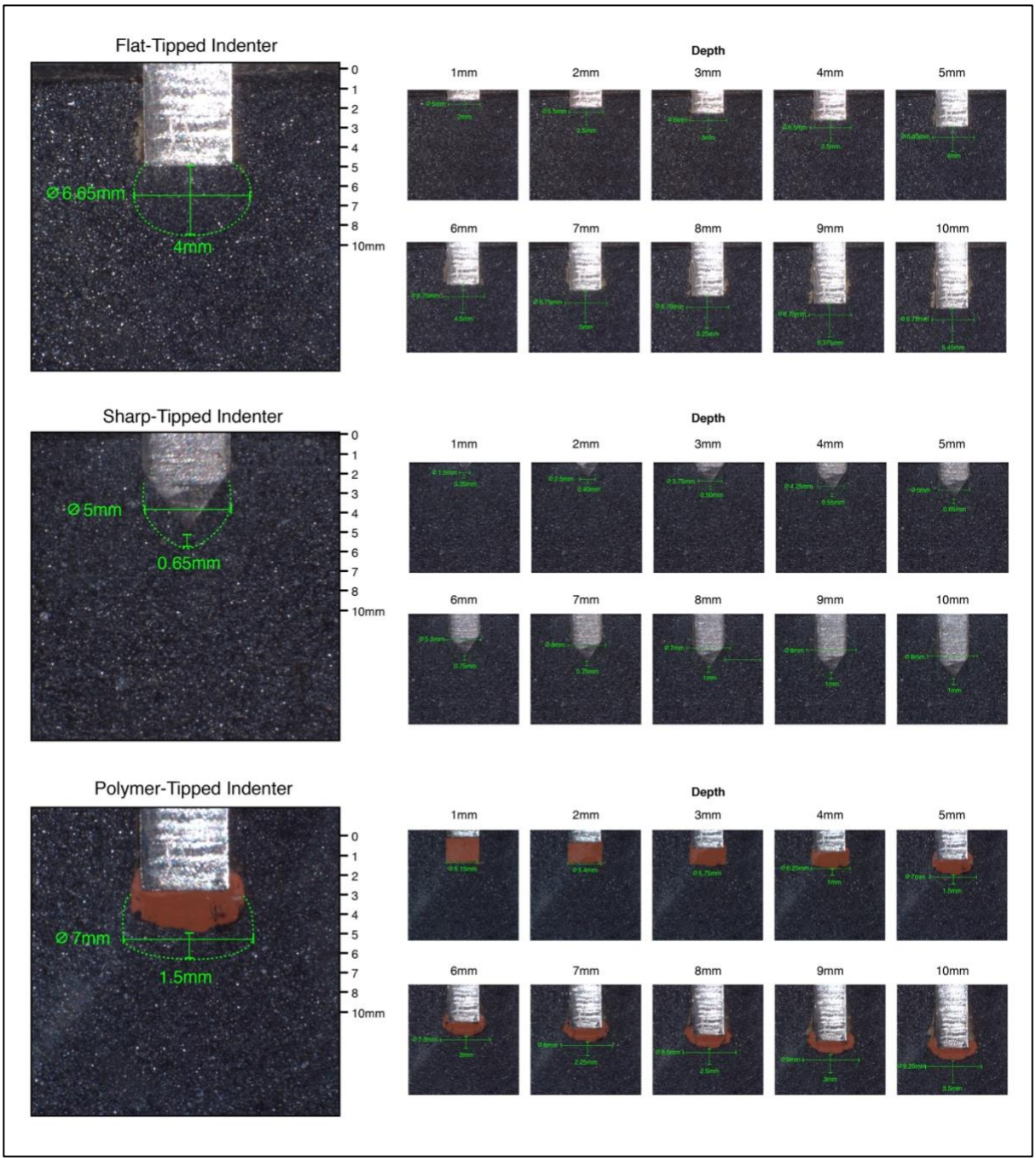

Figure 6. Measurements of compaction zone diameter and length at 1 mm penetration depth intervals. Video still images taken during representative trials of each tip design in implant penetration visualization experiment (half-diameter) (see DiB article,[38] dataset 1.2.2).

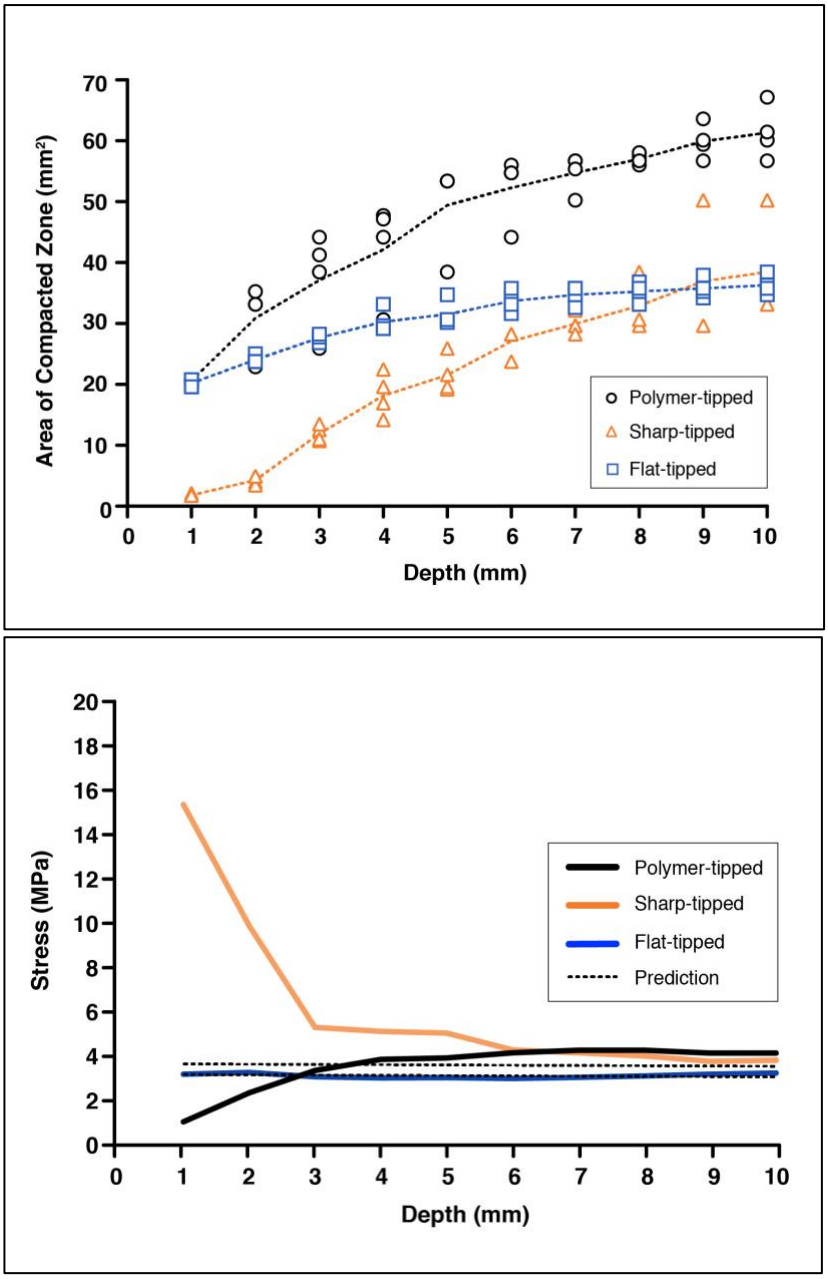

Figure 7. Compaction zone cross-sectional area (top) and mean stress (bottom) vs. depth, for each tip design. Predicted stress refers to range of values generated by analytical model (see DiB article,[38] dataset 1.2.1).

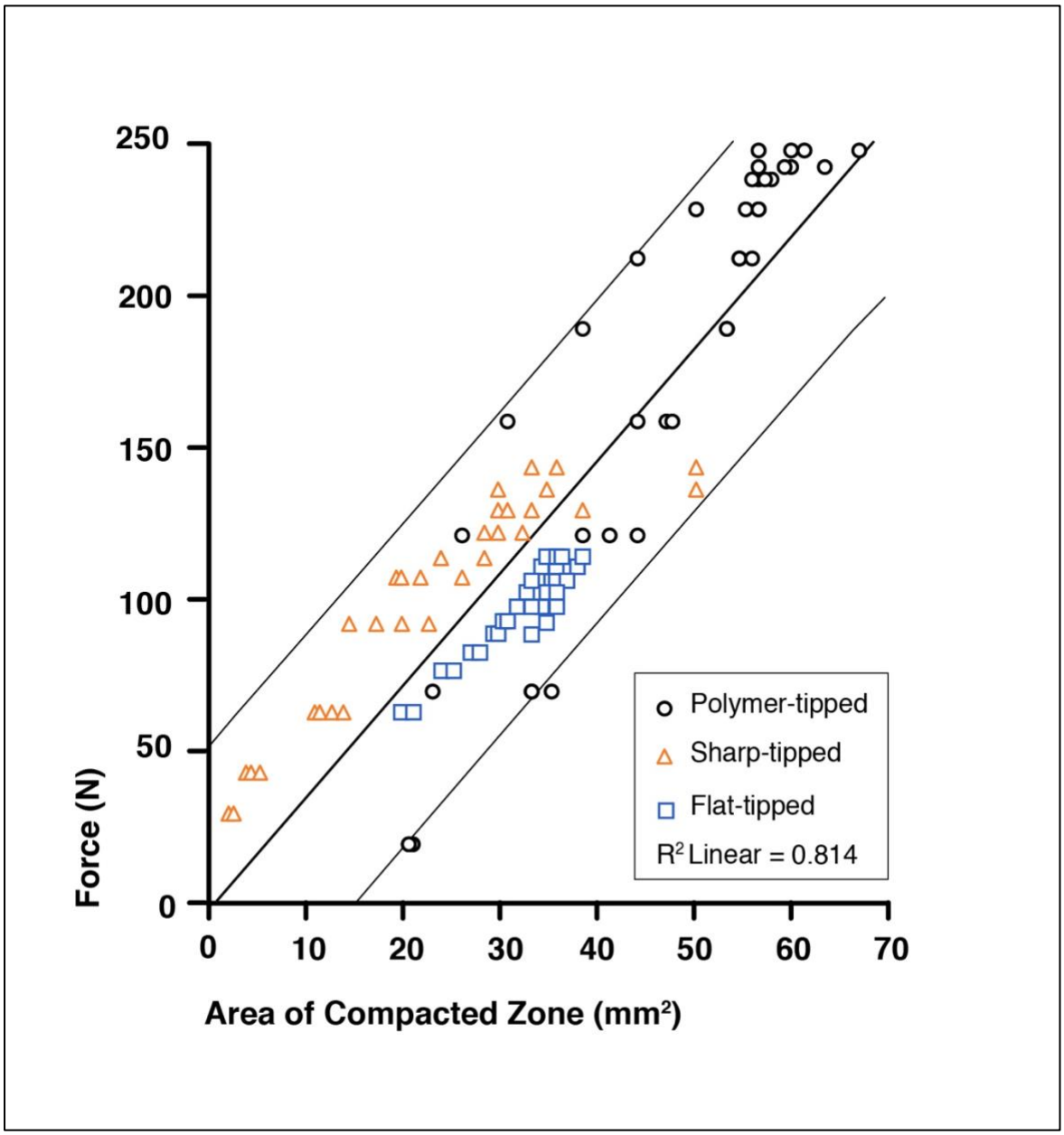

Figure 8. Correlation of compaction zone cross-sectional area and force for each tip design (see DiB article,[38] dataset 1.2.1).

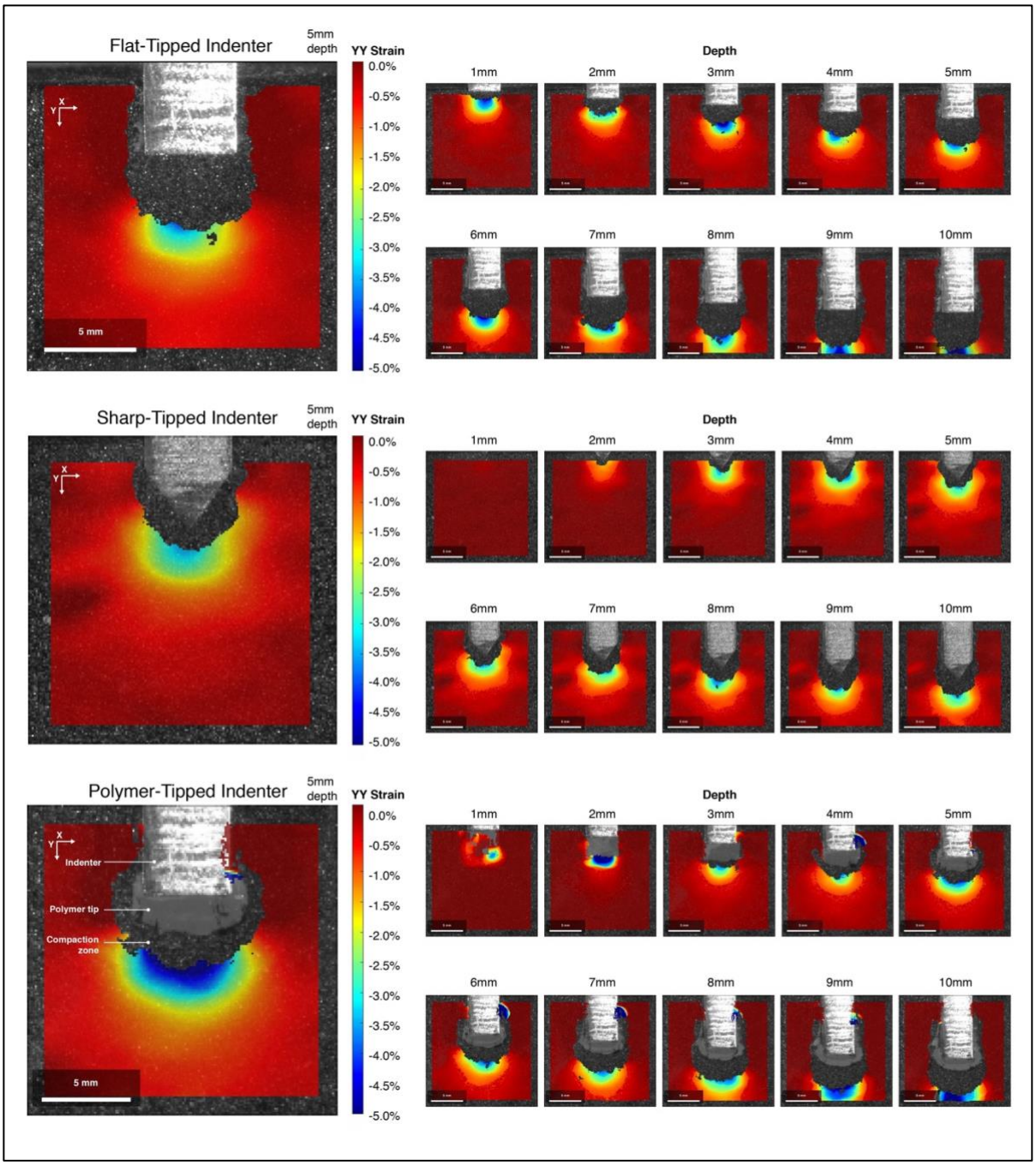

Figure 9. Euler-Almansi YY (vertical) strain fields, generated from video of implant tip penetration visualization experiment using digital image correlation (see DiB article,[38] dataset 1.3.1).

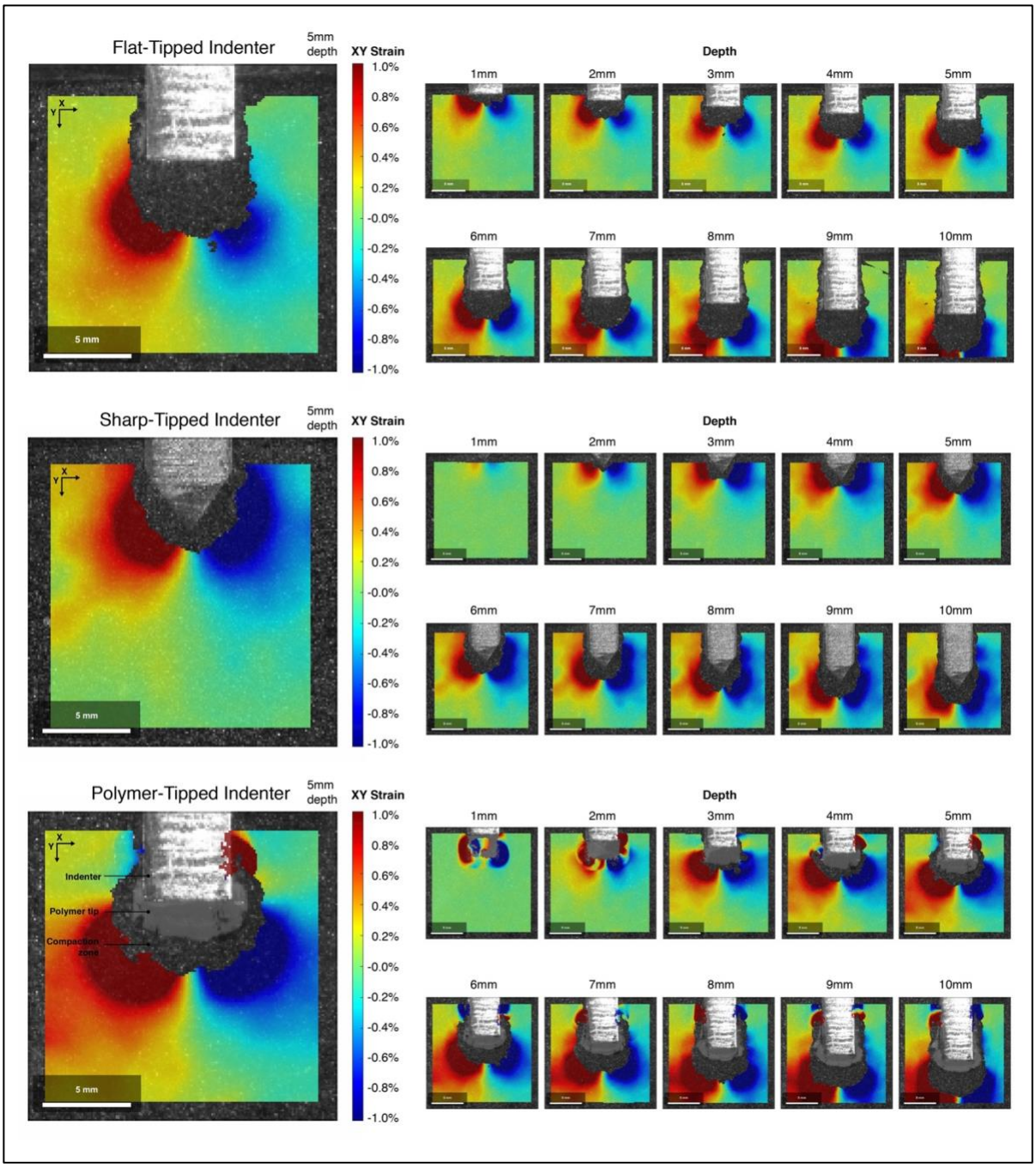

Figure 10. Euler-Almansi XY (shear) strain fields, generated from video of implant tip penetration visualization experiment using digital image correlation (see DiB article,[38] dataset 1.3.1).